processes

MDPI

Article

Well-Log-Interpreted Reservoir Parameters Assisted Evaluation of Hydrophobically Modified Partially Hydrolyzed Polyacrylamide Flooding for Enhanced Oil Recovery in Heterogeneous Reservoirs

Xuanhua Zhang [1,*], Xinmin Ge [1], Rumin Liu [2] and Fan Zhang [3]

[1] School of Geosciences, China University of Petroleum (East China), Qingdao 266580, China; gexinmin2002@upc.edu.cn
[2] China Oilfield Services Limited, Tianjin 300451, China
[3] The Fifth Oil Production Plant of Changqing Oilfield, Xi'an 710200, China
* Correspondence: zhangxh_ii@126.com

Abstract

Polymer flooding is an important enhanced oil recovery technology for high-water-cut heterogeneous reservoirs, where long-term waterflooding commonly leads to preferential flow channels and insufficient mobilization of remaining oil in less-swept intervals. In this study, a hydrophobically modified partially hydrolyzed polyacrylamide-type polymer containing hydrophobic associative groups was evaluated for mobility control and enhanced oil recovery in heterogeneous porous media with the assistance of well-log-interpreted reservoir parameters. Reservoir heterogeneity was first characterized using interpreted effective thickness, porosity, permeability, oil saturation, and water saturation, and the polymer performance was then examined through rheological measurements, core-flooding experiments, and field production response analysis. The results show that the representative reservoir layers exhibit a wide permeability range of 7.9–186.5 mD, with higher water saturation in high-permeability layers and higher oil saturation in medium- and low-permeability layers. The polymer solution shows concentration-dependent thickening, shear-thinning behavior, salinity tolerance, and thermal-aging stability, retaining a viscosity of 139.5 mPa·s at 180,000 mg/L salinity and 74.9% viscosity retention after aging for 504 h. Core-flooding results indicate that the medium-permeability core achieves the highest polymer incremental recovery of 14.5 ± 0.8%, reflecting a favorable balance between injectivity and residual flow resistance. Field production data further show that daily oil production increases from 11.6 to 20.4 t/d, water cut decreases from 93.1% to 81.6%, and cumulative oil increment reaches 2055 t after polymer injection. The proposed mechanism involves associative thickening, pore-throat-adaptive transport, residual flow resistance, flow-path redistribution, and remaining-oil mobilization. This study establishes a heterogeneity-constrained mobility-control framework linking well-log-interpreted reservoir parameters, permeability-dependent polymer transport, residual flow resistance, and field production response, showing that effective polymer flooding depends on balancing injectivity, flow resistance, and remaining-oil availability rather than maximizing bulk viscosity alone.

Keywords: hydrophobically associating polymer; polymer flooding; enhanced oil recovery; well-log-interpreted parameters; heterogeneous reservoir; mobility control; remaining oil mobilization

Check for updates

Academic Editor: Dicho Stratiev

Received: 26 May 2026
Revised: 24 June 2026
Accepted: 26 June 2026
Published: 1 July 2026

Copyright: © 2026 by the authors. Licensee MDPI, Basel, Switzerland. This article is an open access article distributed under the terms and conditions of the Creative Commons Attribution (CC BY) license.

1. Introduction

Polymer flooding has become one of the most mature chemical enhanced oil recovery methods for high-water-cut reservoirs, especially where long-term waterflooding has created severe flow-path heterogeneity and a large amount of remaining oil [1,2]. In heterogeneous sandstone reservoirs, injected water preferentially advances through high-permeability channels, while medium- and low-permeability intervals are often contacted less efficiently. This uneven sweep pattern leads to early water breakthrough, rapid water-cut increase, and inefficient utilization of the oil retained in less-swept zones [3,4]. The essential function of polymer flooding is to increase the viscosity of the injected aqueous phase, reduce the water–oil mobility ratio, and improve macroscopic sweep efficiency [1,2]. However, in high-water-cut reservoirs with strong permeability contrast, polymer flooding cannot be evaluated only from bulk-solution viscosity. Whether the polymer can propagate through the pore-throat system, establish residual flow resistance, and redirect later injected water toward under-swept regions is equally important for enhanced oil recovery [5,6].

Partially hydrolyzed polyacrylamide (HPAM) remains the most widely used polymer in field-scale polymer flooding because of its availability, cost advantage, and viscosity-building ability [1,7]. Nevertheless, conventional HPAM systems may suffer from viscosity loss under high salinity, elevated temperature, mechanical shear, and divalent-ion-rich brines, which limits their application in harsher reservoir conditions [7,8]. Previous studies on HPAM flooding under high-salinity or high-temperature/high-salinity conditions have shown that electrolyte screening, polymer coil contraction, divalent cation interactions, and thermal/mechanical degradation can reduce the hydrodynamic volume of polymer chains and weaken viscosity retention, thereby limiting mobility-control efficiency in harsh brines [9,10]. However, these studies mainly emphasize solution stability and viscosity retention, while the connection among high-salinity tolerance, pore-throat transport, residual resistance formation, and permeability-dependent recovery response remains insufficiently clarified. Hydrophobically associating polymers introduce a small fraction of hydrophobic groups into water-soluble polymer chains, enabling transient intermolecular association in aqueous solution [11]. Such association can enhance viscosity, improve salt tolerance, generate shear-responsive flow behavior, and increase residual flow resistance in porous media [11,12]. Recent studies have shown that hydrophobically associating polymers and other functional polymer systems can improve polymer performance in high-salinity reservoirs, offshore oilfields, and heterogeneous porous media [12,13]. However, stronger viscosity or a higher resistance factor does not necessarily correspond to better oil recovery. Excessive flow resistance may reduce injectivity and limit deep propagation, whereas insufficient resistance may fail to modify preferential water channels [6,14].

Current studies on polymer flooding have provided substantial understanding of polymer rheology, viscoelasticity, salt tolerance, mobility control, and residual oil displacement [14,15]. However, three issues remain insufficiently connected. First, many material-centered studies focus on solution viscosity, shear stability, or salinity tolerance, but do not fully link these properties with permeability-dependent transport in porous media [15,16]. Second, core-flooding studies often report recovery increments, resistance factor, or residual resistance factor, but the relationship among injectivity, residual flow resistance, and incremental recovery under different permeability conditions is still not sufficiently clarified [6,16]. Third, reservoir-scale heterogeneity is often described separately from laboratory flooding results, and the linkage among well-log-interpreted reservoir parameters, core-scale mobility control, and field production response remains weak [3,17]. As a result, the mechanism of hydrophobically associating polymer flooding in heterogeneous reservoirs is still frequently simplified as viscosity enhancement, while the coupled

effects of pore-throat adaptation, residual flow resistance, flow-path redistribution, and remaining-oil mobilization require further clarification.

Based on this, this study evaluates the enhanced oil recovery mechanism of hydrophobically associating polymer flooding in a heterogeneous reservoir with the assistance of well-log-interpreted reservoir parameters. Representative reservoir layers were first characterized using effective thickness, porosity, permeability, oil saturation, and water saturation. The polymer solution was then evaluated through rheological and reservoir-condition stability measurements, followed by permeability-dependent core-flooding experiments and production-dynamic analysis. Rather than focusing only on polymer performance screening, this work aims to clarify how a field-used hydrophobically associating polymer functions under reservoir heterogeneity constraints. The novelty of this study lies in integrating well-log-interpreted reservoir parameters with core-scale mobility-control indicators and field production response to evaluate polymer flooding as a coupled reservoir–fluid–porous-media process. Specifically, this work addresses three mechanistic questions that are not resolved by routine polymer-performance evaluation: whether favorable polymer rheology can be translated into effective pore-throat transport, whether stronger flow resistance necessarily leads to higher incremental recovery, and whether laboratory-observed permeability-dependent mobility control is consistent with field-scale production behavior. The objectives of this work are to clarify the relationship among reservoir heterogeneity, polymer rheology, pore-throat transport, residual flow resistance, and remaining-oil mobilization, and to establish a mechanism framework for hydrophobically associating polymer flooding in high-water-cut heterogeneous reservoirs. This study aims to provide guidance for polymer selection, concentration optimization, and target-layer screening in field-scale mobility-control applications.

Highlights

- Well-log parameters were linked with polymer-flooding performance.
- A hydrophobically modified HPAM-type polymer was evaluated.
- Mobility control depended on pore-throat accessibility.
- Medium-permeability cores showed the highest recovery increment.
- Field response supported polymer-induced flow redistribution.

2. Experimental Section

2.1. Reservoir Background and Well-Log-Interpreted Parameters

The target interval was selected from a high-water-cut heterogeneous sandstone reservoir that had undergone long-term waterflooding before polymer treatment. Previously interpreted well-log parameters, including effective thickness, porosity, permeability, oil saturation, water saturation, and reservoir classification, were used to characterize reservoir heterogeneity and guide permeability-dependent experimental design. The original logging curves were not reprocessed in this work.

Representative layers were selected to cover high-, medium-, and low-permeability intervals. Layers with permeability higher than 100 mD were classified as high-permeability layers, those with permeability of approximately 40–100 mD were classified as medium-permeability layers, and those with permeability lower than 30 mD were classified as low-permeability layers. Oil and water saturation values were used to describe the pre-polymer displacement status of each layer, rather than as direct evidence of polymer-flooding performance. The well-log-interpreted parameters of the representative reservoir layers are summarized in Table 1.

Table 1. Well-log-interpreted parameters of representative reservoir layers used for heterogeneity characterization.

Layer	Depth Top/m	Effective Thickness/m	Porosity/%	Permeability/mD	Oil Saturation/%	Water Saturation/%	Reservoir Type
L1	2136.4	2.4	18.9	148.6	45.8	54.2	High-permeability
L2	2141.8	3.7	16.7	72.4	56.4	43.6	Medium-permeability
L3	2149.6	1.9	13.4	24.8	63.7	36.3	Low-permeability
L4	2156.2	5.2	19.6	186.5	43.2	56.8	High-permeability
L5	2164.7	2.8	11.8	9.7	68.9	31.1	Low-permeability
L6	2173.5	4.6	15.2	46.3	60.5	39.5	Medium-permeability
L7	2181.9	3.1	10.6	7.9	70.3	29.7	Low-permeability
L8	2190.3	5.7	17.8	105.2	50.6	49.4	High-permeability

The selected parameters were used to characterize reservoir heterogeneity in terms of storage capacity, flow capacity, fluid-saturation status, and layer-scale contribution to flow. Effective thickness was used to represent the scale of each reservoir interval, porosity and permeability were used to describe storage and flow properties, and oil and water saturation were used to indicate the pre-polymer displacement status of each layer. Because these parameters represent layer-specific interpretation results rather than replicated laboratory measurements, they were treated as deterministic reservoir-characterization data in the heterogeneity analysis.

2.2. Materials and Experimental Apparatus

The hydrophobically associating polymer was supplied by Beijing Hengju Chemical Group Co., Ltd. (Beijing, China) as a white to light-yellow powder and was used without further purification. The polymer was a hydrophobically modified partially hydrolyzed polyacrylamide-type water-soluble polymer. Its molecular structure consisted mainly of an acrylamide/acrylate backbone containing a small fraction of hydrophobic associative monomer units. The partially hydrolyzed carboxylate groups provided an anionic charge character under the experimental pH condition of 7.0–7.5, whereas the hydrophobic side groups enabled transient interchain association in aqueous solution. Therefore, the polymer performance was controlled by both electrostatic hydration of the anionic segments and reversible hydrophobic association among polymer chains. Its basic properties are summarized in Table 2.

Analytical-grade NaCl (≥99.5%), $CaCl_2$ (≥96.0%), $MgCl_2{\cdot}6H_2O$ (≥98.0%), and $NaHCO_3$ (≥99.5%) were purchased from Sinopharm Chemical Reagent Co., Ltd. (Shanghai, China). Synthetic formation water was prepared by dissolving these salts in deionized water. The standard brine salinity was 100,000 mg/L, and brines with salinities of 0, 50,000, 100,000, 150,000, and 180,000 mg/L were prepared for salinity stability tests. The pH was maintained at 7.0–7.5. The crude oil was obtained from the target reservoir block, dehydrated, and filtered before use; its viscosity at 85°C was 9.8 ± 0.3 mPa·s, as measured using the MCR 302 rotational rheometer equipped with a concentric cylinder geometry. The measurement temperature was consistent with that used in the core-flooding experiments, and the reported value represents the average of three repeated measurements. This value was used as the oil-phase viscosity reference for evaluating the mobility contrast during polymer flooding.. Artificial sandstone cores were supplied by Haian Petroleum Scientific Research Instrument Co., Ltd. (Nantong, China).

Table 2. Basic properties of the hydrophobically associating polymer used in this study.

Property	Value
Polymer type	Hydrophobically associating polymer
Chemical category	Hydrophobically modified partially hydrolyzed polyacrylamide-type polymer
Supplier	Beijing Hengju Chemical Group Co., Ltd., Beijing, China
Appearance	White to light-yellow powder
Solid content/%	90.6
Apparent molecular weight/10^6 g/mol	8.5
Hydrolysis degree/%	22.8
Hydrophobic monomer content/mol%	0.48
Main structural feature	Acrylamide/acrylate water-soluble backbone containing a small fraction of hydrophobic associative monomer units
Charge character	Anionic, mainly originating from partially hydrolyzed carboxylate groups
Zeta potential at pH 7.0–7.5/mV	-18.4 ± 1.1
Associative mechanism	Transient interchain hydrophobic association combined with electrostatic hydration of anionic chain segments
Standard concentration/wt%	0.25
Dissolution time/h	12

Rheological measurements were performed using an MCR 302 rotational rheometer (Anton Paar GmbH, Graz, Austria) equipped with a concentric cylinder geometry. The zeta potential of the polymer solution was measured using a Zetasizer Nano ZS analyzer (Malvern Panalytical Ltd., Malvern, UK) after dilution to 0.01 wt% with synthetic formation water at pH 7.0–7.5. Each measurement was repeated three times, and the result was reported as mean ± standard deviation. Thermal aging was conducted in a DHG-9140A thermostatic oven (Shanghai Yiheng Scientific Instrument Co., Ltd., Shanghai, China). Core-flooding experiments were carried out using a high-temperature core-flooding system equipped with an ISCO 260D syringe pump (Teledyne ISCO, Lincoln, NE, USA), a stainless-steel core holder, a confining-pressure unit, a back-pressure regulator, a differential-pressure transducer, and a produced-fluid collection system. Core mass was measured using an ME204E electronic balance (Mettler Toledo, Zurich, Switzerland), and vacuum saturation was performed using a 2XZ-4 rotary vane vacuum pump (Shanghai Yoke Instrument Co., Ltd., Shanghai, China).

2.3. Preparation of Hydrophobically Associating Polymer Solutions

The polymer solution was prepared using a stepwise hydration procedure. A predetermined mass of polymer powder was slowly added to synthetic formation water under continuous stirring, with the powder introduced along the vortex wall to minimize local agglomeration. For the standard solution, the polymer concentration was fixed at 0.25 wt%. This concentration was selected to match the field injection design concentration used in the polymer-flooding treatment and was also included in the laboratory rheological screening range. Based on the nonlinear increase in apparent viscosity and the strengthened shear-thinning response observed above 0.15 wt%, the apparent critical association concentration, or association threshold, was inferred to be approximately 0.15–0.20 wt%. Therefore, the selected 0.25 wt% concentration was above this apparent association threshold and was expected to form a developed associative network. The concentration-dependent shear-rate sweep tests from 0.05 to 0.30 wt% were used to verify whether the selected concentration could provide a representative shear-thinning response and a sufficient rheological basis for mobility control without using an excessively high polymer dosage. Therefore, 0.25 wt%

was used as the standard concentration for salinity stability, thermal aging, injectivity, and oil displacement evaluations, rather than as an arbitrarily selected laboratory concentration. The mixture was stirred at 400 r/min for 2 h, sealed, and aged at 25 °C for 12 h to ensure complete hydration. Before testing, the solution was gently stirred at 150 r/min for 20 min and then allowed to stand for 30 min to remove visible bubbles.

Polymer solutions with concentrations of 0.05, 0.10, 0.15, 0.20, 0.25, and 0.30 wt% were prepared for concentration-dependent rheological tests. For salinity stability tests, 0.25 wt% polymer solutions were prepared in brines with salinities of 0–180,000 mg/L. For thermal aging tests, the standard 0.25 wt% polymer solution prepared in 100,000 mg/L synthetic formation water was sealed in glass bottles before aging.

2.4. Rheological and Reservoir-Condition Stability Measurements

The rheological behavior of the hydrophobically associating polymer solution was evaluated using a rotational rheometer equipped with a concentric cylinder geometry. The measurement temperature was maintained at 25 °C for concentration-dependent and shear-rate tests unless otherwise specified. In addition, the standard 0.25 wt% polymer solution was measured at 85 °C under the same shear-rate range to provide a reservoir-temperature rheological reference consistent with the core-flooding experiments. Before each test, the polymer solution was gently homogenized and equilibrated at the target temperature for 10 min. Each test was repeated three times, and the data were reported as mean ± standard deviation.

For concentration-dependent rheological evaluation, polymer solutions with concentrations of 0.05, 0.10, 0.15, 0.20, 0.25, and 0.30 wt% were subjected to shear-rate sweep tests over 0.10–200 s^{-1}, rather than being evaluated only at a single shear rate. The apparent viscosity at 7.34 s^{-1} was retained only as a standardized reference value for comparing concentration-dependent thickening behavior. Because the polymer solutions exhibited non-Newtonian shear-thinning behavior, the shear-stress data were further fitted using the Herschel–Bulkley model:

$$\tau = \tau_0 + K\dot{\gamma}^n$$

where τ is the shear stress, τ_0 is the apparent yield stress, K is the consistency index, $\dot{\gamma}$ is the shear rate, and n is the flow behavior index. The fitted parameters were used to describe the concentration dependence of polymer rheology more appropriately than a single apparent-viscosity value.

However, this fixed shear rate was used only as a standardized rheological reference and was not assumed to represent the actual shear rate inside the porous media. To link the bulk rheological data with core-scale transport behavior, the apparent average pore shear rate was further estimated for each permeability class in the core-flooding analysis.

For the shear-rate response test, the standard 0.25 wt% polymer solution was measured over a shear-rate range of 0.10–200 s^{-1}. The shear rate was increased stepwise, and the apparent viscosity was recorded after the reading became stable at each point. For continuous rheological curves, the mean value was calculated from three repeated measurements, and the variation range was expressed using standard deviation.

The salinity stability of the polymer solution was evaluated by preparing 0.25 wt% polymer solutions in brines with salinities of 0, 50,000, 100,000, 150,000, and 180,000 mg/L. After complete hydration, the viscosity was measured at 7.34 s^{-1} and 25°C. The viscosity retention was calculated as follows:

$$\text{Viscosity retention}(\%) = \frac{\eta_t}{\eta_0} \times 100$$

where η_t is the viscosity of the polymer solution under a given salinity or aging condition, and η_0 is the reference viscosity before treatment.

Thermal-aging stability was evaluated by sealing the 0.25 wt% polymer solution in glass bottles and aging it at 85 °C for 0, 24, 72, 168, 336, and 504 h. After aging, the samples were cooled to room temperature and gently homogenized before viscosity measurement at 7.34 s^{-1}. The viscosity retention after aging was calculated using the equation above.

2.5. Core-Flooding Procedure and Mobility-Control Evaluation

Core-flooding experiments were conducted to evaluate polymer injectivity, flow-resistance regulation, and oil-displacement performance under different permeability conditions. Artificial sandstone cores were used to represent high-, medium-, and low-permeability porous media. The physical properties of representative cores are summarized in Table 3. Each permeability class was tested in triplicate using three separate core samples with similar permeability and porosity, and statistical results were reported as mean ± standard deviation where applicable. The triplicate experiments were used to calculate statistical indicators, including end-point pressure gradient, RF, RRF, residual-to-dynamic resistance ratio, and recovery indicators.

Table 3. Physical properties of core samples used for core-flooding experiments.

Core Permeability Class	Representative Permeability/mD	Length/cm	Diameter/cm	Porosity/%	Pore Volume/mL
High-permeability core	146.8	6.0	2.5	19.2	5.65
Medium-permeability core	48.5	6.0	2.5	15.8	4.65
Low-permeability core	13.9	6.0	2.5	12.4	3.65

To relate the shear-thinning behavior measured by rheometry to polymer transport in porous media, the apparent average pore shear rate was estimated using a capillary-bundle approximation:

$$\dot{\gamma}_{av} = \frac{4u}{\sqrt{8k\phi}}$$

where $\dot{\gamma}_{av}$ is the apparent average pore shear rate, u is the Darcy velocity calculated from the injection rate and core cross-sectional area, k is the core permeability in m^2, and ϕ is the porosity expressed as a fraction. At an injection rate of 0.30 mL/min and a core diameter of 2.5 cm, the Darcy velocity was 1.02×10^{-5} m/s. The estimated average pore shear rates were 86.4, 165.6, and 349.3 s^{-1} for the high-, medium-, and low-permeability cores, respectively. These values were used as apparent shear-rate references to interpret viscosity reduction and pressure buildup during polymer transport, rather than as exact local pore-scale shear rates. The estimated apparent average pore shear rates for cores with different permeability classes are summarized in Table 4.

Table 4. Estimated apparent average pore shear rates in cores with different permeability classes.

Core Permeability Class	Permeability/mD	Porosity/%	Darcy Velocity/m·s^{-1}	Estimated Average Pore Shear Rate/s^{-1}
High-permeability core	146.8	19.2	1.02×10^{-5}	86.4
Medium-permeability core	48.5	15.8	1.02×10^{-5}	165.6
Low-permeability core	13.9	12.4	1.02×10^{-5}	349.3

Two flooding protocols were used to separately evaluate polymer injectivity and oil-displacement performance. For the injectivity test, each core was first subjected to water

preflush from 0 to 0.40 PV to establish a stable baseline pressure. The 0.25 wt% polymer solution was then injected from 0.40 to 0.90 PV, and the pressure difference across the core was continuously recorded to characterize polymer transport and pressure buildup. This protocol was used to compare the pressure response of high-, medium-, and low-permeability cores during polymer migration.

For the oil-displacement test, the flooding process consisted of three stages. First, waterflooding was conducted from 0 to 0.80 PV to establish the baseline displacement behavior. The recovery at 0.80 PV was used as the recovery level at the start of polymer injection, rather than as the ultimate waterflooding recovery. Second, 0.25 wt% polymer solution was injected from 0.80 to 1.10 PV. The polymer slug size was therefore 0.30 PV. This slug size was selected based on the field injection design experience of the target well group and the need to maintain a consistent pore-volume-normalized comparison among cores with different permeabilities. It was not determined from an independent polymer adsorption, retention, or effluent-concentration breakthrough test. Third, post-polymer waterflooding was conducted from 1.10 to 1.70 PV. The polymer-related incremental recovery was therefore evaluated from the recovery increase after 0.80 PV, together with the water-cut response and the final stage-based recovery contribution. The 0.60 PV post-polymer waterflooding stage was included to capture delayed oil mobilization and residual flow-resistance effects after polymer passage. Because polymer breakthrough and retention volumes were not directly measured in this work, the 0.30 PV slug should be interpreted as a field-relevant comparative slug size rather than an optimized or breakthrough-confirmed slug size. Produced oil and water were collected at fixed intervals to calculate oil recovery and water cut. All flooding experiments were performed at 85 °C with a constant injection rate of 0.30 mL/min. The pressure difference across the core was continuously recorded using a differential-pressure transducer. During the core-flooding experiments, the confining pressure was maintained at 8.0 MPa to ensure radial sealing and to prevent bypass flow along the core surface. The pressure values reported in the pressure response curves represent the differential pressure across the core rather than the absolute inlet pressure or the confining pressure. Therefore, the end-point pressure and pressure gradient were used only to evaluate core-scale injectivity and polymer-induced flow resistance under the imposed laboratory boundary conditions. They were not directly used as reservoir-scale fracture-pressure indicators.

Oil recovery was calculated as the ratio of cumulative produced oil to the original oil in place:

$$\text{Oil recovery}/\% = V_{\text{op}}/V_{\text{OI}} \times 100$$

where V_{op} is the cumulative produced oil volume, and V_{OI} is the original oil volume in the core. Water cut was calculated as:

$$\text{Water cut}/\% = V_{\text{w}}/(V_{\text{w}} + V_{\text{o}}) \times 100$$

where V_{w} and V_{o} are the produced water and oil volumes collected during each sampling interval, respectively. Polymer incremental recovery was calculated as the difference between final recovery and waterflooding recovery.

The resistance factor (RF) and residual resistance factor (RRF) were calculated to quantify polymer-induced flow resistance:

$$\text{RF} = \Delta P_{\text{p}}/\Delta P_{\text{w1}}$$

$$\text{RRF} = \Delta P_{\text{w2}}/\Delta P_{\text{w1}}$$

where ΔP_{w1} is the stable pressure difference during water preflush before polymer injection, ΔP_p is the stable pressure difference during polymer injection, and ΔP_{w2} is the stable pressure difference during post-polymer waterflooding. For each independent core-flooding run, ΔP_{w1}, ΔP_p, and ΔP_{w2} were determined from the corresponding stable pressure plateau, and RF and RRF were calculated separately for that run. Therefore, the error bars of RF and RRF represent the standard deviation of three independently calculated values for each permeability class, rather than repeated pressure readings from a single core-flooding curve. The residual-to-dynamic resistance ratio was calculated as RRF/RF × 100%. This ratio was used as an auxiliary indicator to compare the fraction of polymer-induced resistance retained after polymer passage. The end-point pressure gradient was calculated by dividing the end-point pressure by the core length.

Representative dynamic curves were selected to describe the flooding process, while end-point pressure gradient, RF, RRF, and recovery indicators were calculated from triplicate experiments for each permeability class. Process curves were presented as representative experimental records, whereas statistical indicators were expressed as mean ± standard deviation. This distinction was made because the continuous pressure and recovery curves show representative displacement behavior, whereas the bar charts and summary indicators reflect the statistical results from three independent core-flooding experiments.

2.6. Production-Dynamic Data and Field-Scale Evaluation

The cumulative oil increment was estimated by comparing the actual oil production after polymer injection with the predicted baseline production in the absence of polymer treatment. The baseline production was established by fitting a linear decline trend to the daily oil production data collected during the six months before polymer injection. The start of polymer injection was defined as month 0, and the fitted decline trend was extrapolated over the post-polymer monitoring period to obtain the predicted oil production without polymer treatment. This approach was selected because the pre-polymer monitoring period was relatively short and the production decline during this period showed an approximately linear trend. To examine the sensitivity of the cumulative oil increment to the baseline-decline model, an exponential decline baseline was also calculated as a comparative check:

$$Q_{o,base}(t) = Q_{o0}e^{-Dt}$$

where Q_{o0} is the daily oil production at the start of polymer injection, D is the exponential decline constant, and t is the time after polymer injection in months. The value of D was estimated from the six-month pre-polymer production trend using $D = \ln(Q_{o,-6}/Q_{o0})/6$, where $Q_{o,-6}$ and Q_{o0} are the daily oil production rates at six months before polymer injection and at month 0, respectively. This exponential baseline was used only for sensitivity analysis of the reported field oil increment, not as an additional mechanistic proof of polymer flooding.

The oil increment for each monitoring interval was calculated from the difference between actual and baseline daily oil production. The cumulative oil increment was then obtained by summing the interval oil increments:

$$\text{Cumulative oil increment} = \Sigma\,(Q_{o,\text{actual}} - Q_{o,\text{baseline}}) \times \Delta t$$

where $Q_{o,\text{actual}}$ is the actual daily oil production after polymer injection, $Q_{o,\text{baseline}}$ is the predicted daily oil production under the pre-polymer decline trend, and Δt is the production time interval. Only positive differences were included in the cumulative increment calculation to avoid attributing natural production fluctuation or short-term operational disturbance to polymer flooding. This calculation was used to evaluate the field-scale

production response and was not treated as independent evidence of the microscopic displacement mechanism.

3. Results and Discussion

3.1. Reservoir Heterogeneity Characterized by Well-Log-Interpreted Parameters

To clarify the reservoir-scale heterogeneity before polymer flooding and provide a basis for the subsequent permeability-dependent evaluation, representative layers were characterized using well-log-interpreted petrophysical parameters. Figure 1 summarizes the corresponding variations in porosity, permeability, fluid saturation, and effective thickness.

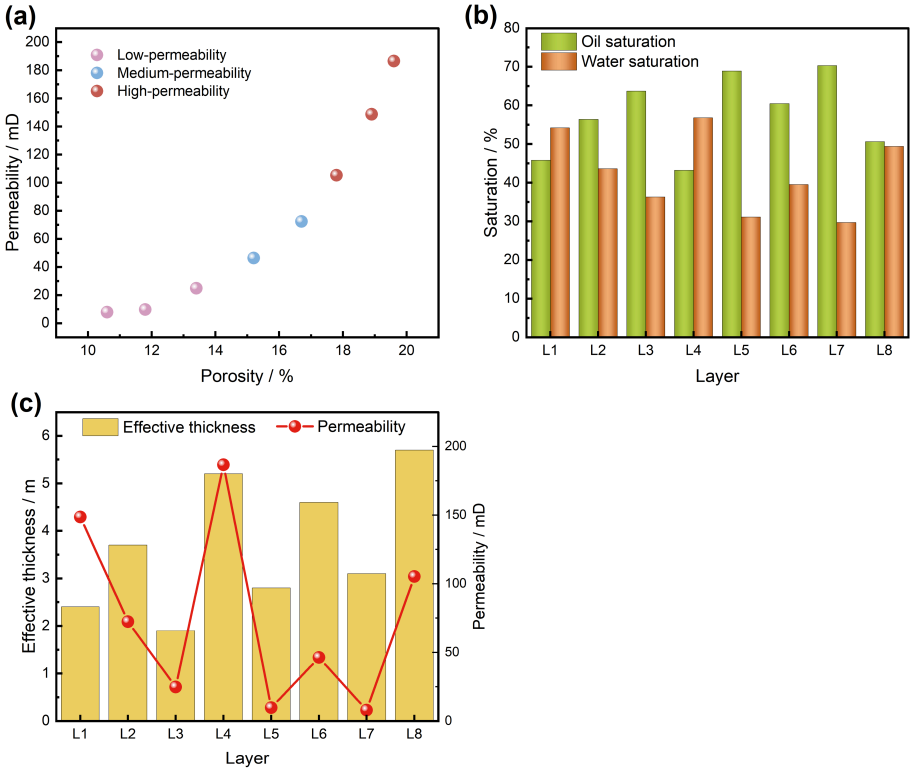


Figure 1. Reservoir heterogeneity characterized by well-log-interpreted parameters: (**a**) porosity–permeability relationship of representative layers; (**b**) oil and water saturation distribution; (**c**) effective thickness and permeability of different layers.

The porosity–permeability cross-plot in Figure 1a shows that the representative layers covered a relatively narrow porosity interval but a much wider permeability range. Porosity ranged from 10.6% to 19.6%, whereas permeability varied from 7.9 to 186.5 mD. Layers L1, L4, and L8 were classified as high-permeability intervals, with permeability values of 148.6, 186.5, and 105.2 mD, respectively. L2 and L6 fell within the medium-permeability range, while L3, L5, and L7 represented the low-permeability layers. The permeability contrast was not fully explained by porosity. For example, L2 and L8 had relatively close porosity values, but their permeability differed noticeably. This mismatch points to the role of pore-throat connectivity in controlling flow capacity, rather than storage volume alone.

The saturation profile in Figure 1b gives a further indication of uneven displacement after long-term water flooding. High-permeability layers generally had higher water saturation, with L1 and L4 reaching 54.2% and 56.8%, respectively. This pattern is consistent with preferential water movement through more conductive intervals. By contrast, the low-permeability layers retained higher oil saturation, with values of 63.7% for L3, 68.9% for L5, and 70.3% for L7. The contrast between high-water-saturation conductive layers and

oil-retaining tighter layers suggests that the previous waterflooding stage did not sweep the reservoir section uniformly.

When effective thickness is compared with permeability in Figure 1c, the potential contribution of different layers to preferential flow becomes clearer. L4 combined a relatively large effective thickness of 5.2 m with the highest permeability of 186.5 mD, while L8 had the largest effective thickness of 5.7 m and a permeability of 105.2 mD. These two layers may therefore contribute more strongly to dominant flow paths during water injection. L6, with an effective thickness of 4.6 m and a permeability of 46.3 mD, represents a medium-permeability interval that still retained an oil saturation of 60.5%. Compared with tighter low-permeability layers, this type of interval may offer a more favorable combination of polymer accessibility and remaining-oil potential.

The combined information from Figure 1a–c defines the reservoir context for polymer-flooding evaluation. High-permeability intervals appear to have been more strongly affected by water invasion, whereas medium- and low-permeability layers retained higher oil saturation. This contrast does not directly prove the subsequent polymer-flooding mechanism, but it identifies the type of heterogeneity in which mobility control may become relevant. Therefore, the polymer solution first needed to be evaluated for its rheological stability and ability to provide a flow-resistance basis under reservoir-relevant conditions.

3.2. Rheological Behavior and Reservoir-Condition Stability of the Hydrophobically Associating Polymer

To evaluate whether the hydrophobically associating polymer could provide a stable fluid-property basis for mobility control, its viscosity response was examined under concentration, shear-rate, salinity, and thermal-aging conditions. Because the polymer solutions behaved as non-Newtonian fluids, the concentration effect was evaluated not only by apparent viscosity at a standardized shear rate, but also by shear-rate-dependent rheological curves and fitted model parameters. The rheological and stability results are shown in Figure 2. Error bars or shaded regions represent the standard deviation from three independent measurements.

The shear-rate-dependent viscosity curves of polymer solutions with different concentrations are shown in Figure 2a. All polymer solutions exhibited shear-thinning behavior, and the apparent viscosity decreased continuously as the shear rate increased from 0.10 to 200 s^{-1}. Increasing polymer concentration shifted the viscosity curves upward over the entire shear-rate range, indicating stronger intermolecular association and chain entanglement at higher polymer concentrations. Therefore, the concentration effect should not be interpreted only from a single apparent-viscosity value, but from the combined shear-rate response and fitted rheological parameters. For comparison with the original concentration screening, the apparent viscosity at the standardized shear rate of 7.34 s^{-1} increased from 14.8 mPa·s at 0.05 wt% to 63.2 mPa·s at 0.15 wt%, and further increased to 186.2 and 286.7 mPa·s at 0.25 and 0.30 wt%, respectively. This nonlinear increase reflects the enhanced probability of intermolecular association as polymer chains become more concentrated in solution. The sharper viscosity increase above 0.15 wt% suggests that the apparent association threshold of the polymer solution was reached within approximately 0.15–0.20 wt%. Therefore, the standard concentration of 0.25 wt% was above this apparent CAC range, supporting the formation of an associative network that could contribute to viscosity enhancement, pore-throat interaction, and residual flow resistance.

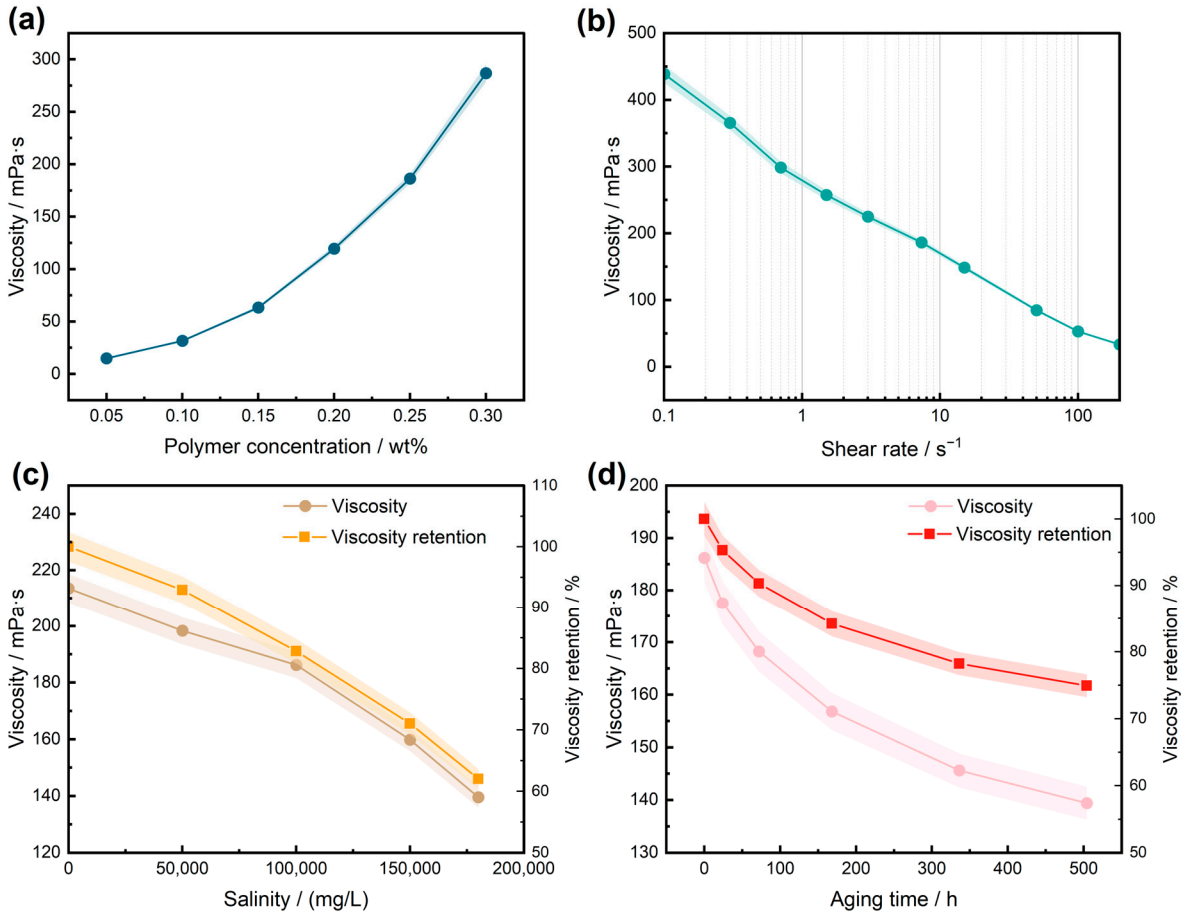


Figure 2. Rheological behavior and reservoir-condition stability of the hydrophobically associating polymer: (**a**) shear-rate-dependent viscosity curves of polymer solutions with different concentrations; (**b**) shear-rate response of the standard 0.25 wt% polymer solution; (**c**) salinity stability; and (**d**) thermal-aging stability. Data are presented as mean ± SD (n = 3); the shaded region in panel (**b**) represents the standard-deviation range.

To further quantify the non-Newtonian rheological behavior, the shear-stress data were fitted using the Herschel–Bulkley model. The fitted parameters are summarized in Table 5. With increasing polymer concentration from 0.05 to 0.30 wt%, the consistency index K increased from 0.018 to 0.760 Pa·s^n, while the flow behavior index n decreased from 0.84 to 0.45. This trend indicates that higher polymer concentrations strengthened the pseudoplastic character of the solution. The apparent yield stress τ_0 also increased gradually with concentration, suggesting the formation of a stronger weak-network structure associated with hydrophobic association and chain entanglement. The 0.25 wt% solution had a fitted K of 0.410 Pa·s^n, n of 0.52, and τ_0 of 0.190 Pa, indicating a clear shear-thinning response while maintaining manageable flowability for injection.

The shear-rate curve in Figure 2b shows that the 0.25 wt% polymer solution behaved as a shear-thinning fluid. Viscosity decreased from 438.6 mPa·s at 0.10 s^{-1} to 186.2 mPa·s at 7.34 s^{-1}, and further declined to 33.4 mPa·s at 200 s^{-1}. This confirms that the viscosity reported at 7.34 s^{-1} should be regarded as a standardized comparison value rather than a constant viscosity independent of shear conditions. This response is relevant to injection because the solution may experience relatively high shear near the wellbore and lower shear after entering deeper porous media. The decrease in viscosity under high shear is likely associated with partial chain stretching, disentanglement, and temporary disruption of associative structures. The shaded standard-deviation band remained narrow along the

curve, supporting the reproducibility of the shear-response trend. To improve consistency with the 85 °C core-flooding experiments, the standard 0.25 wt% polymer solution was also tested at 85 °C. At 7.34 s^{-1}, its apparent viscosity decreased from 186.2 mPa·s at 25 °C to 118.6 ± 4.1 mPa·s at 85 °C, indicating temperature-induced viscosity reduction. Nevertheless, this viscosity remained much higher than the crude oil viscosity at 85 °C, suggesting that the polymer solution could still provide a reservoir-temperature viscosity basis for mobility control.

Table 5. Herschel–Bulkley fitting parameters of polymer solutions with different concentrations.

Polymer Concentration/wt%	Apparent Yield Stress τ_0/Pa	Consistency Index K/Pa·s^n	Flow Behavior Index n	R^2
0.05	0.006	0.018	0.84	0.993
0.10	0.018	0.046	0.78	0.994
0.15	0.055	0.112	0.69	0.995
0.20	0.110	0.220	0.61	0.996
0.25	0.190	0.410	0.52	0.997
0.30	0.320	0.760	0.45	0.997

According to the apparent pore shear-rate estimation in Table 4, the polymer solution experienced a higher shear-rate range in the cores than the standardized 7.34 s^{-1} used for viscosity comparison. Therefore, the viscosity measured at 7.34 s^{-1} should be regarded as a standardized rheological reference rather than the actual in-core viscosity during polymer migration. The estimated shear-rate range indicates that the polymer solution likely underwent additional shear-induced viscosity reduction during core flooding, especially in the medium- and low-permeability cores. Nevertheless, the core-scale mobility-control capability was evaluated not only from bulk viscosity, but also from pressure response, RF, RRF, and oil-displacement performance.

Salinity stability was evaluated to determine whether the associating structure could retain viscosity under mineralized conditions. In Figure 2c, viscosity retention decreased from 100.0% in deionized water to 92.9%, 82.8%, 71.0%, and 62.0% as salinity increased to 50,000, 100,000, 150,000, and 180,000 mg/L, respectively. The viscosity remained at 139.5 mPa·s even at 180,000 mg/L, suggesting that the polymer retained part of its thickening capacity under highly mineralized conditions. Ionic screening may compress hydrated polymer coils and weaken chain expansion, whereas hydrophobic association appears to preserve a certain contribution to solution viscosity.

The thermal-aging profile in Figure 2d shows a gradual viscosity loss rather than an abrupt collapse. Viscosity retention decreased from 100.0% to 95.3% after 24 h and remained at 84.2% after 168 h. After aging for 504 h, the retention was still 74.9%, with a measured viscosity of 139.4 mPa·s. The gradual decrease may be related to thermal relaxation of polymer chains and partial weakening of associative interactions, but the remaining viscosity indicates that the solution maintained a usable viscosity level during the aging period.

These rheological responses define a practical fluid-property window for porous-media flooding. The polymer solution exhibited concentration-dependent shear-rate response, non-Newtonian shear-thinning behavior, salinity tolerance, and thermal-aging stability within the tested range. The Herschel–Bulkley fitting results further show that increasing polymer concentration enhanced the consistency index and apparent yield stress while reducing the flow behavior index, confirming that concentration mainly strengthened the weak-network and pseudoplastic characteristics of the polymer solution. These properties do not directly demonstrate oil recovery improvement, but they provide the

necessary basis for examining whether additional flow resistance can be established after the polymer enters porous media. The next section therefore examines whether this rheological potential can be translated into injectivity and mobility-control behavior in cores with different permeability levels.

3.3. Core-Scale Injectivity and Mobility Control in Heterogeneous Porous Media

3.3.1. Pressure Response and Injectivity During Polymer Transport

To evaluate the injectivity of the hydrophobically associating polymer in porous media with different permeability levels, pressure variations were recorded during water preflush and subsequent polymer injection. The pressure response and end-point pressure-gradient results are shown in Figure 3.

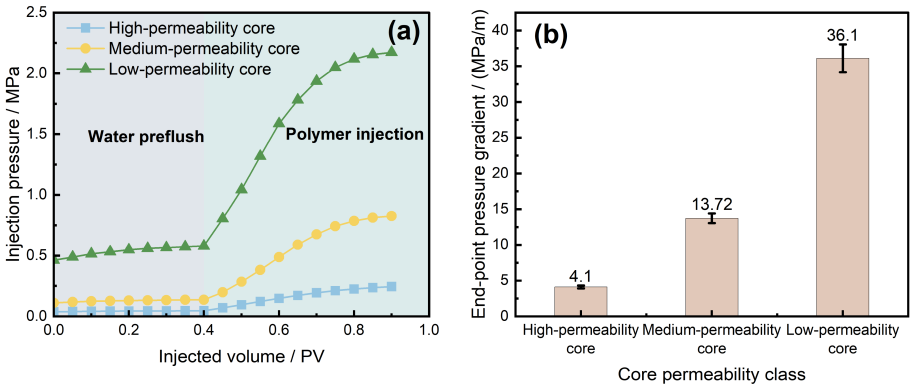


Figure 3. Pressure response and injectivity during polymer transport: (**a**) representative pressure records during water preflush and polymer injection; (**b**) end-point pressure gradient in cores with different permeability classes. Data in panel (**b**) are presented as mean ± SD (n = 3).

The pressure profiles in Figure 3a show a clear transition from stable water flow to polymer-induced pressure buildup. During the water-preflush stage from 0 to 0.40 PV, the pressure in each core remained relatively stable, indicating that a baseline flow state had been established before polymer injection. Once the polymer solution entered the cores, the pressure increased in all permeability classes, but the magnitude of the increase depended strongly on core permeability.

In the high-permeability core, the pressure increased gradually from approximately 0.047 MPa at the end of water preflush to 0.245 MPa at 0.90 PV. This smooth buildup suggests that the polymer solution could propagate through the more conductive pore network while introducing measurable additional flow resistance. The medium-permeability core showed a stronger pressure response, with pressure increasing from 0.137 to 0.826 MPa over the same injection interval. The curve remained smooth, which does not support abrupt plugging but reflects a stronger interaction between polymer transport and pore-throat restriction.

The low-permeability core behaved differently, with pressure increasing from 0.578 MPa at the end of water preflush to 2.172 MPa at 0.90 PV. This higher pressure level points to a less favorable injectivity condition, most likely associated with narrower pore throats and stronger resistance to polymer propagation. It should be noted that the recorded pressure was the differential pressure across the 6.0 cm core, rather than the absolute injection pressure. Under the applied confining pressure of 8.0 MPa, the maximum differential pressure of 2.172 MPa did not approach the confining-pressure boundary used in the core holder. In addition, the pressure curve increased progressively without a sudden pressure drop, pressure oscillation, or flow interruption, which does not support macroscopic core fracturing or unstable channel opening during the test. The absence

of a sudden vertical pressure jump suggests that complete plugging was not observed under the tested condition. Even so, the much higher pressure level indicates that polymer transport in low-permeability porous media was more restricted than in the medium- and high-permeability cores.

The end-point pressure gradients in Figure 3b provide a compact comparison of injectivity among the three permeability classes. The pressure gradient increased from 4.10 ± 0.20 MPa/m in the high-permeability core to 13.72 ± 0.68 MPa/m in the medium-permeability core and 36.10 ± 1.93 MPa/m in the low-permeability core. The relatively small standard deviations show that this permeability-dependent pressure response was reproducible in repeated tests. Although the pressure gradient in the low-permeability core was high, it was a core-scale gradient calculated over a short laboratory core length and should not be directly compared with reservoir fracture pressure. Rather, it indicates severe pore-throat restriction, enhanced local shear, and limited polymer accessibility in tight porous media. Therefore, the low-permeability response was interpreted as restricted polymer propagation with strong flow resistance, not as evidence of more efficient deep mobility control. Compared with the low-permeability core, the medium-permeability core developed a clear pressure increase while maintaining a much lower pressure gradient, suggesting a more workable balance between polymer transport and injectivity.

These pressure responses indicate that polymer injectivity cannot be judged only from solution viscosity. A moderate pressure increase can be useful because it reflects the formation of additional flow resistance in the pore network. Excessive pressure buildup, however, may restrict deep propagation and reduce the effective swept volume. The high-pressure gradient in the low-permeability core also implies that shear-induced viscosity reduction or localized polymer retention may be more pronounced under tighter pore-throat conditions. This possibility is consistent with the shear-rate sensitivity discussed above and was considered when interpreting the RF, RRF, and oil-displacement results. For this reason, the following section further examines RF and RRF to distinguish transient flow resistance during polymer injection from the residual resistance retained during subsequent waterflooding.

3.3.2. Resistance Factor and Residual Flow Resistance

To further quantify the flow-resistance regulation caused by polymer transport, the resistance factor (RF) and residual resistance factor (RRF) were calculated from the pressure responses before, during, and after polymer injection. The results are shown in Figure 4.

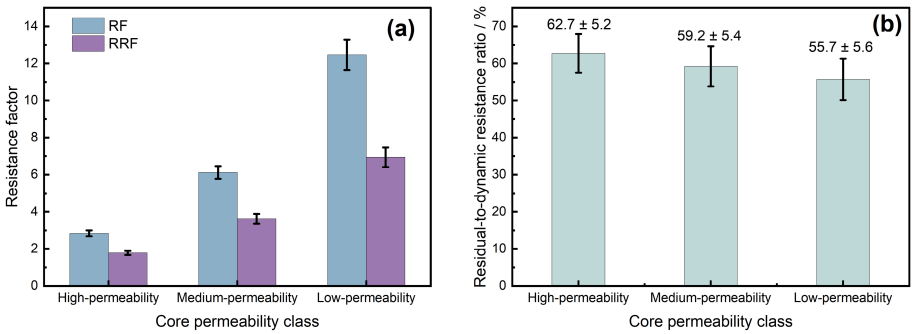


Figure 4. Resistance factor and residual flow resistance in heterogeneous cores: (**a**) resistance factor (RF) and residual resistance factor (RRF) under different permeability conditions; (**b**) residual-to-dynamic resistance ratio calculated from RRF/RF. Error bars represent the standard deviation of three independent core-flooding experiments for each permeability class. In panel (**b**), the SD values for the high-, medium-, and low-permeability cores were 5.2%, 5.4%, and 5.6%, respectively. Data are presented as mean ± SD (n = 3).

The RF and RRF comparison in Figure 4a shows that polymer-induced flow resistance increased as core permeability decreased. The high-permeability core had an RF of 2.84 ± 0.16, indicating a moderate increase in flow resistance during polymer injection. In the medium-permeability core, RF increased to 6.12 ± 0.34, reflecting a stronger interaction between the polymer solution and the pore-throat system. The low-permeability core showed the highest RF of 12.46 ± 0.82. This high value is consistent with the pressure buildup observed in Figure 3, but it should not be equated directly with better mobility control because excessive resistance may limit polymer propagation in tighter pore networks.

RRF followed the same permeability-dependent trend, but the values were lower than the corresponding RF values. The RRF values were 1.78 ± 0.11, 3.62 ± 0.26, and 6.94 ± 0.53 for the high-, medium-, and low-permeability cores, respectively. The difference between RF and RRF reflects the partial loss of dynamic resistance after the polymer slug passed through the core, while the remaining RRF confirms that part of the polymer-induced resistance persisted during subsequent waterflooding. Such residual resistance may be associated with polymer retention, adsorption, or mechanical restriction within pore throats, although the pressure-based data do not separate these contributions.

The residual-to-dynamic resistance ratio in Figure 4b provides a useful way to compare the retained fraction of polymer-induced flow resistance. The ratio decreased slightly from 62.7 ± 5.2% in the high-permeability core to 59.2 ± 5.4% and 55.7 ± 5.6% in the medium- and low-permeability cores, respectively. Although the differences among the three cores were not large, all ratios exceeded 55%, showing that a considerable portion of the polymer-induced resistance remained after polymer transport. The standard deviations of 5.2–5.6% also indicate acceptable repeatability of this derived parameter.

These results refine the injectivity interpretation obtained from the pressure response analysis. The medium-permeability core developed a clear increase in RF and RRF without reaching the excessive pressure-gradient level observed in the low-permeability core. This response points to a more favorable balance between polymer accessibility and residual flow-resistance formation. By contrast, the stronger resistance in the low-permeability core may reflect restricted transport rather than efficient deep mobility control. The following oil-displacement evaluation therefore examines whether these differences in flow resistance can be translated into measurable incremental recovery.

3.4. Enhanced Oil Recovery Performance Under Permeability-Dependent Conditions

To examine whether the flow resistance generated by the hydrophobically associating polymer could be translated into oil-displacement improvement, core-flooding experiments were conducted using high-, medium-, and low-permeability cores. The oil recovery, water-cut response, and recovery contribution are shown in Figure 5.

The recovery profiles in Figure 5a show that the initial waterflooding response was strongly affected by core permeability. At 0.80 PV, the high-permeability core reached a waterflooding recovery of 55.1%, whereas the medium- and low-permeability cores reached 46.2% and 31.4%, respectively. It should be emphasized that the recovery at 0.80 PV represents the recovery level at the start of polymer injection, not the ultimate recovery obtainable by extended waterflooding. Therefore, Figure 5a was used mainly to show the continuous displacement history and the timing of the polymer slug, rather than to prove polymer effectiveness from an abrupt break in the cumulative recovery curve. The higher waterflooding recovery in the high-permeability core reflects easier fluid access and lower flow resistance. The lower recovery in the low-permeability core is consistent with a more restricted pore-throat system, where injected water was less able to contact the oil phase efficiently.

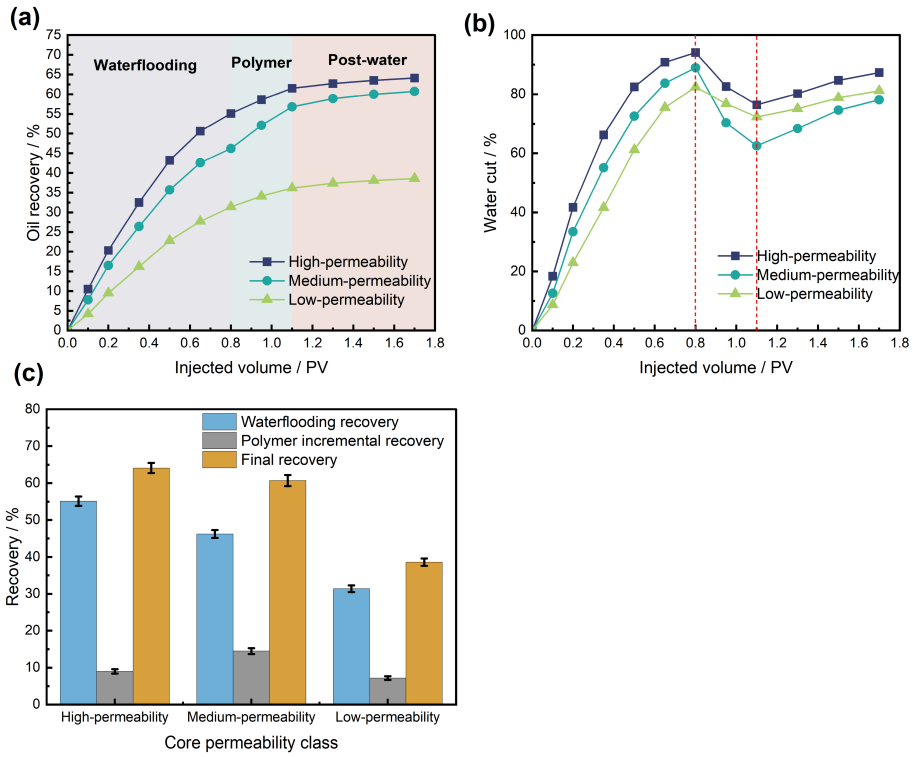


Figure 5. Enhanced oil recovery performance under permeability-dependent conditions: (**a**) cumulative oil recovery evolution during initial waterflooding, polymer injection, and post-polymer waterflooding; (**b**) water-cut response during the displacement process; (**c**) stage-based recovery contribution, including recovery at the start of polymer injection, polymer/post-polymer incremental recovery, and final recovery in cores with different permeability classes. Vertical dashed lines in panel (**a**) indicate the transition points at 0.80 PV and 1.10 PV. Data in panel (**c**) are presented as mean ± SD (n = 3).

The recovery at 0.80 PV represents the recovery level at the start of polymer injection, and the polymer/post-polymer incremental recovery was calculated as the difference between final recovery at 1.70 PV and recovery at 0.80 PV. Because cumulative oil recovery curves are inherently smooth, the polymer effect may not appear as a sharp slope break immediately after polymer injection. Polymer-induced mobility control can produce a delayed response through flow-resistance buildup, residual resistance formation, and post-polymer flow redistribution. Therefore, the oil-displacement improvement was evaluated using the stage-based recovery contribution in Table 6 and the water-cut response in Figure 5b, rather than relying solely on the visual shape of Figure 5a.

Table 6. Stage-based recovery contribution during core flooding.

Core Permeability Class	Recovery at 0.80 PV/%	Final Recovery at 1.70 PV/%	Polymer/Post-Polymer Incremental Recovery/%
High-permeability core	55.1	64.1 ± 1.4	9.0 ± 0.6
Medium-permeability core	46.2	60.7 ± 1.5	14.5 ± 0.8
Low-permeability core	31.4	38.6	7.2 ± 0.5

As summarized in Table 6 and Figure 5c, polymer injection and subsequent waterflooding increased recovery in all cores, but the incremental response did not increase monotonically with permeability. The medium-permeability core showed the largest polymer/post-polymer incremental recovery of 14.5 ± 0.8%, increasing the final recovery to 60.7 ± 1.5%. The high-permeability core had a smaller increment of 9.0 ± 0.6%, although

its final recovery reached 64.1 ± 1.4%. This behavior suggests that a considerable fraction of movable oil in the high-permeability core had already been produced during the initial waterflooding stage, leaving less oil available for polymer-assisted mobilization. The low-permeability core showed an incremental recovery of 7.2 ± 0.5%, which is consistent with restricted polymer propagation inferred from the higher pressure-gradient response.

It should be noted that the 0.30 PV polymer slug was not designed to determine the maximum attainable incremental recovery. Because polymer adsorption, retention, and effluent breakthrough were not independently measured, the possibility that the selected slug size was smaller than the full retention-controlled propagation volume cannot be excluded. This effect would be more pronounced in the low-permeability core, where stronger pore-throat restriction and higher pressure buildup indicate more limited polymer propagation. Therefore, the incremental recovery reported here should be interpreted as the recovery response under a fixed, field-relevant comparative slug size. It may represent a conservative estimate of the recoverable polymer-induced increment, particularly for tighter porous media, rather than the absolute maximum recovery obtainable at larger polymer slug sizes.

The water-cut curves in Figure 5b provide additional evidence for permeability-dependent flow redistribution. Before polymer injection, water cut increased rapidly in all cores, especially in the high-permeability core, where it reached 94.1% at 0.80 PV. During polymer injection, water cut decreased to 76.4% in the high-permeability core and to 62.5% in the medium-permeability core at 1.10 PV. The low-permeability core showed a smaller decrease, from 82.4% to 72.3%. The more pronounced water-cut reduction in the medium-permeability core is consistent with a more effective modification of the displacement path, whereas polymer propagation in the low-permeability core remained more constrained. Thus, the evidence for polymer-induced improvement is reflected more clearly by the stage-based recovery increment and the water-cut reduction than by an abrupt change in the cumulative recovery curve.

Figure 5c separates the contributions of waterflooding and polymer flooding under different permeability conditions. In this revised interpretation, the term "waterflooding recovery" refers to the recovery at the start of polymer injection after 0.80 PV of initial waterflooding, rather than the ultimate waterflooding recovery. High permeability favored waterflooding recovery, but the largest polymer-induced increment occurred in the medium-permeability core. This contrast suggests that effective polymer flooding requires both remaining-oil availability and sufficient polymer accessibility. A highly conductive pore network may already be strongly swept by water, while an excessively tight pore network may restrict polymer transport. Under the present experimental conditions, the medium-permeability core provided a more favorable balance between these two factors.

The oil-displacement results are consistent with the pressure and flow-resistance observations in Sections 3.3.1 and 3.3.2. The low-permeability core generated a high pressure gradient and RF, but this did not translate into the highest incremental recovery. The medium-permeability core, by contrast, combined moderate pressure buildup, clear residual flow resistance, and the largest polymer incremental recovery. These results support the view that the EOR performance of the hydrophobically associating polymer was controlled by permeability-dependent transport and mobility regulation, rather than by solution viscosity or flow resistance alone.

3.5. Production Response and Field-Scale Consistency

To examine whether the laboratory-observed mobility-control behavior was reflected in field production response, the dynamic performance before and after polymer injection was analyzed using production and injection records from the target well group. The

changes in daily oil production, water cut, injection pressure, cumulative polymer injection, and cumulative oil increment are shown in Figure 6.

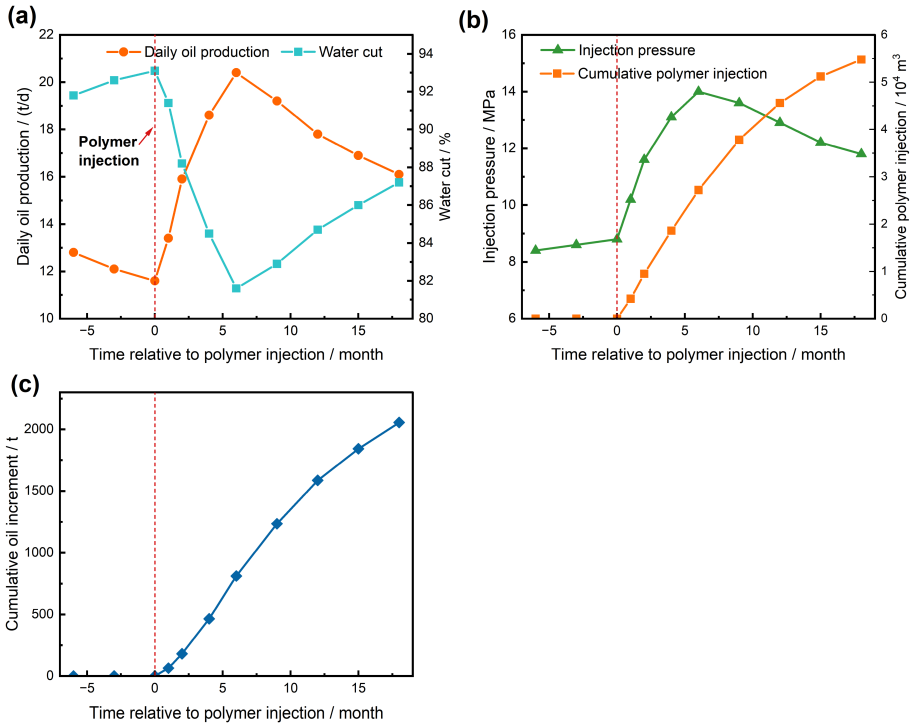


Figure 6. Production response and field-scale consistency relative to polymer injection: (**a**) daily oil production and water cut; (**b**) injection pressure and cumulative polymer injection volume; (**c**) cumulative oil increment. Negative values on the *x*-axis denote the months before polymer injection, and month 0 marks the start of polymer injection. Error bars are not included because the curves represent field production records rather than replicated laboratory measurements.

The production profile in Figure 6a shows that the well group was already in a high-water-cut stage before polymer injection. During the six months before treatment, daily oil production decreased from 12.8 to 11.6 t/d, while water cut increased from 91.8% to 93.1%. After polymer injection started, oil production increased gradually and reached 20.4 t/d at 6 months. Over the same period, water cut declined to 81.6%. The opposite movement of oil production and water cut is consistent with a change in flow-path distribution, although production data alone cannot resolve the pore-scale displacement process.

The injection-side response in Figure 6b gives additional information on how the reservoir responded to polymer placement. Injection pressure increased from 8.8 MPa at month 0 to 14.0 MPa at 6 months, accompanied by a cumulative polymer injection volume of 2.72×10^4 m^3. The pressure did not continue rising after this point; instead, it gradually decreased to 11.8 MPa at 18 months, while cumulative polymer injection reached 5.48×10^4 m^3. This non-monotonic pressure trajectory can be interpreted as a two-stage reservoir response to polymer injection. During the early injection stage, the polymer solution preferentially entered the dominant water-conducting pathways and increased flow resistance through viscosity enhancement, polymer retention, and residual resistance formation. This process increased injection pressure and helped suppress part of the previously dominant water-flow channels. During the later stage, once additional resistance had been established in the preferential pathways, the injected fluid was redistributed toward a broader set of flow paths, including previously less-swept intervals. The resulting injection-profile adjustment and reservoir pressure redistribution likely increased

the effective flow capacity of the injection system, leading to a gradual pressure decline despite continued polymer injection.

This pressure decrease is therefore not interpreted as evidence of continuously intensifying plugging. It is also not sufficient, by itself, to prove near-wellbore plugging removal or localized fracturing, because no abrupt pressure drop, pressure oscillation, injection interruption, or sudden deterioration of the production response was observed in the available field records. Near-wellbore shear thinning or partial mechanical degradation of the polymer may have contributed to the reduction in apparent flow resistance, but these effects could not be separated quantitatively from the present field data. Therefore, the most likely explanation is pressure redistribution following polymer-induced injection-profile adjustment, with near-wellbore shear effects being a possible secondary contribution.

The cumulative oil increment in Figure 6c increased slowly during the first two months and then rose more rapidly between 4 and 12 months. The cumulative oil increment reached 812 t at 6 months, 1586 t at 12 months, and 2055 t at 18 months. Such a delayed and progressive response matches the time required for polymer propagation and flow redistribution in the reservoir. This field-scale behavior is also in line with the core-flooding results, where polymer transport generated residual flow resistance rather than acting only as a bulk-viscosity enhancer.

Because the calculated field oil increment depends on the assumed baseline decline trend, an exponential-decline sensitivity check was further conducted to evaluate the robustness of the reported 18-month cumulative oil increment. Based on the pre-polymer daily oil production decreasing from 12.8 to 11.6 t/d over six months, the exponential decline constant was estimated as 0.0163 month^{-1}. When the exponential baseline was used instead of the linear baseline, the cumulative oil increment at 18 months was approximately 1890 t. This corresponds to a relative deviation of about −8.0% compared with the 2055 t obtained from the linear baseline, as summarized in Table 7. Therefore, the field-scale oil-increment estimate was moderately affected by the baseline-decline model, but the positive production response remained robust under the exponential-decline sensitivity check.

Table 7. Sensitivity of cumulative field oil increment to baseline-decline model.

Baseline-Decline Model	Estimated Cumulative Oil Increment at 18 Months/t	Relative Deviation from Linear Baseline/%
Linear decline baseline	2055	0
Exponential decline baseline	1890	−8.0

Among the core-scale responses discussed above, the field behavior more closely resembles the balanced response observed in the medium-permeability core. In both cases, additional flow resistance was established without causing an uncontrollable pressure increase, and the reduction in water cut was accompanied by improved oil production. This comparison supports the importance of balancing injectivity and mobility control: excessive resistance may restrict deep propagation, whereas insufficient resistance may fail to divert flow away from dominant channels.

The production response should be viewed as field-scale consistency rather than independent proof of the microscopic displacement mechanism. In addition, the cumulative oil increment should be interpreted as a model-dependent field estimate rather than an absolute value independent of baseline selection. When considered together with the core-scale pressure, resistance, and recovery results, the field data support a permeability-dependent process in which polymer transport, residual flow resistance, and flow redistribution jointly contribute to improved oil recovery.

3.6. Proposed EOR Mechanism of Hydrophobically Associating Polymer Flooding

The mechanistic significance of this study is not limited to confirming that the hydrophobically associating polymer can increase solution viscosity or improve oil recovery. Such responses are expected for polymer-flooding systems and therefore cannot fully explain the permeability-dependent recovery behavior observed in this work. The key finding is that polymer-flooding effectiveness in heterogeneous porous media is governed by a balance among associative thickening, pore-throat accessibility, residual flow resistance, and remaining-oil availability. In this mechanism, the highest flow resistance does not necessarily correspond to the highest incremental oil recovery. Instead, the most favorable EOR response occurs when polymer propagation, residual resistance formation, and movable remaining-oil distribution are sufficiently matched.

To avoid interpreting the EOR mechanism only from a schematic description, the proposed mechanism was further constrained by quantitative evidence obtained from rheological measurements, core-flooding tests, resistance-factor analysis, oil-displacement results, and field production response. Therefore, Figure 7 should be regarded as a data-supported interpretive framework rather than direct pore-scale visualization. The quantitative links between the proposed mechanism and the experimental or field indicators are summarized in Table 8.

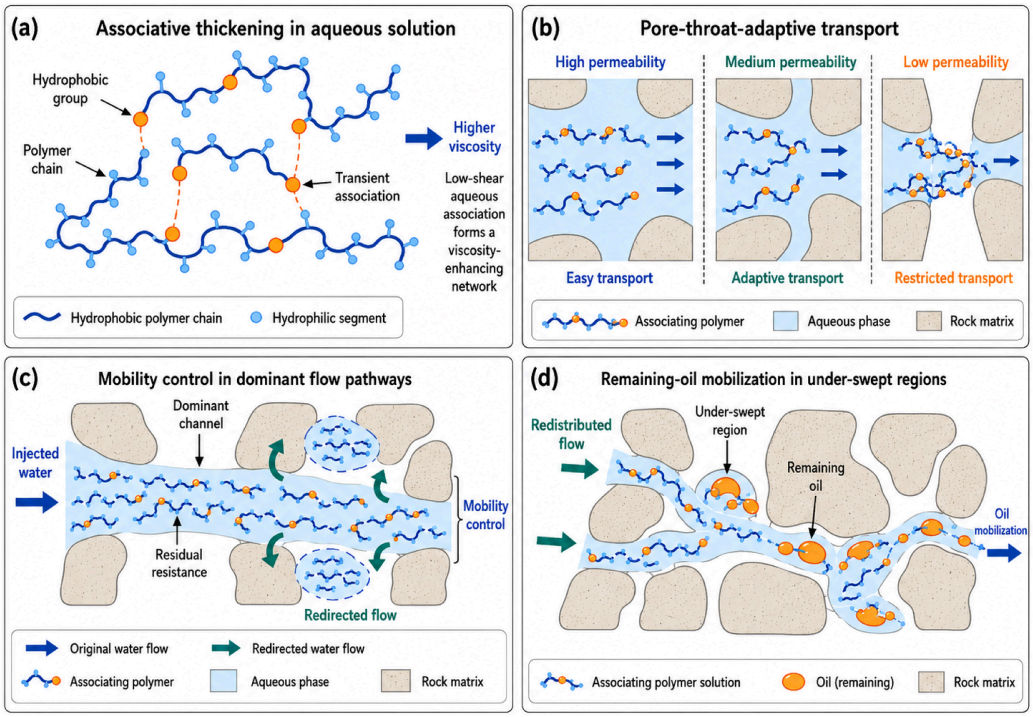


Figure 7. Proposed EOR mechanism of hydrophobically associating polymer flooding in heterogeneous porous media: (**a**) associative thickening in aqueous solution; (**b**) pore-throat-adaptive transport under different permeability conditions; (**c**) mobility control and residual flow resistance in dominant flow pathways; (**d**) remaining-oil mobilization in previously under-swept regions.

The experimental and production responses described above suggest that the EOR behavior of the hydrophobically associating polymer cannot be explained by bulk-solution viscosity alone. Figure 7 summarizes a coupled mechanism in which associative thickening, pore-throat-adaptive transport, and mobility control operate sequentially in heterogeneous porous media.

Table 8. Quantitative evidence supporting the proposed EOR mechanism.

Mechanistic Element	Quantitative Evidence	Mechanistic Interpretation
Associative thickening and shear-responsive transport	The 0.25 wt% polymer solution had a viscosity of 186.2 mPa·s at 7.34 s^{-1}; viscosity decreased from 438.6 mPa·s at 0.10 s^{-1} to 33.4 mPa·s at 200 s^{-1}.	The polymer provided viscosity enhancement under low-to-moderate shear and maintained shear-responsive transportability under high-shear conditions.
Reservoir-condition stability	The viscosity remained 139.5 mPa·s at 180,000 mg/L salinity; viscosity retention after 504 h aging was 74.9%.	The polymer retained a usable viscosity basis under high-salinity and thermal-aging conditions.
Pore-throat-dependent transport	The end-point pressure gradient increased from 4.10 ± 0.20 MPa/m in the high-permeability core to 13.72 ± 0.68 MPa/m in the medium-permeability core and 36.10 ± 1.93 MPa/m in the low-permeability core.	Lower permeability imposed stronger pore-throat restriction and higher resistance to polymer propagation.
Dynamic and residual flow resistance	RF values were 2.84 ± 0.16, 6.12 ± 0.34, and 12.46 ± 0.82; RRF values were 1.78 ± 0.11, 3.62 ± 0.26, and 6.94 ± 0.53 for the high-, medium-, and low-permeability cores, respectively.	Polymer transport generated additional dynamic resistance, and part of this resistance remained during subsequent waterflooding.
Balance between resistance and recovery	Polymer/post-polymer incremental recoveries were 9.0 ± 0.6%, 14.5 ± 0.8%, and 7.2 ± 0.5% for the high-, medium-, and low-permeability cores, respectively.	The strongest resistance did not produce the highest recovery; the medium-permeability core provided the most favorable balance among injectivity, residual resistance, and remaining-oil mobilization.
Field-scale consistency	Daily oil production increased from 11.6 to 20.4 t/d, water cut decreased from 93.1% to 81.6%, and cumulative oil increment reached 2055 t after polymer injection.	The field response was consistent with polymer-induced flow redistribution, but was treated as field-scale consistency rather than independent microscopic proof.

3.6.1. Coupled Effect of Associative Thickening, Pore-Throat Adaptation, and Mobility Control

At the solution scale, the hydrophobically associating polymer forms transient intermolecular associations among hydrophobic groups, which increases apparent viscosity and provides the rheological basis for mobility control. This interpretation is supported by the concentration-dependent rheological response and the Herschel–Bulkley fitting results, which showed that increasing polymer concentration enhanced the consistency index and apparent yield stress while reducing the flow behavior index. However, the core-flooding results show that this bulk-solution effect cannot be directly translated into oil recovery without considering pore-throat transport. During polymer migration, the associating structures may partially stretch, disentangle, or reorganize under shear, allowing the polymer solution to pass through the pore network while still generating additional flow resistance. This pore-throat-adaptive transport is essential for maintaining injectivity and avoiding excessive near-inlet pressure buildup.

In the aqueous phase, hydrophobic groups on polymer chains can form transient intermolecular associations, as illustrated in Figure 7a. This interpretation is consistent with the nonlinear increase in viscosity with polymer concentration and the shear-thinning response observed in Figure 2. The polymer therefore provides viscosity enhancement under relatively low-shear conditions while remaining transportable under higher shear. After entering porous media, this solution behavior is further constrained by pore-throat geometry.

Figure 7b represents this permeability-dependent transport process: wide pore channels allow easier polymer migration, whereas narrow throats increase retention and propagation resistance. This trend agrees with the pressure-gradient response in Figure 3, where lower-permeability cores produced stronger pressure buildup. Using a capillary-bundle approximation based on the permeability and porosity values in Table 3, the estimated equivalent pore-throat radii of the high-, medium-, and low-permeability cores were approximately 2.46, 1.56, and 0.94 μm, respectively. These values should be interpreted as apparent equivalent radii for comparing permeability-dependent confinement effects, rather than directly measured pore-throat sizes. At the physicochemical level, the increased resistance in narrow pore throats is related to hydrodynamic size restriction, chain deformation, transient association, and polymer retention. When the effective pore-throat size approaches the hydrodynamic size of associated polymer coils, polymer chains may stretch, disentangle, and reorganize during passage through constricted throats, which increases local energy dissipation and apparent flow resistance. Meanwhile, weak adsorption on pore walls, cation-mediated interactions under mineralized brine conditions, bridging at pore constrictions, and mechanical entrapment in smaller throats may reduce the effective flow area and increase the pressure gradient required for subsequent water flow. Therefore, pore-throat adaptation should be understood not only as a transport process, but also as a resistance-building process that connects polymer migration with mobility control.

The mobility-control process in Figure 7c is linked to the RF and RRF results. Polymer transport generated additional flow resistance during injection, and part of this resistance remained during subsequent waterflooding. However, the strongest resistance did not correspond to the highest incremental recovery. The medium-permeability core showed a more favorable balance among injectivity and residual resistance. This indicates that the resistance generated in narrow pore throats is beneficial only when it remains compatible with sufficient polymer propagation. If retention and throat restriction become excessive, polymer-induced resistance may be concentrated near the inlet or within limited flow paths, thereby reducing deep mobility control and limiting additional oil mobilization. This comparison indicates that effective polymer flooding depends on a workable balance between polymer accessibility and flow-resistance regulation, rather than on maximizing viscosity or resistance alone.

3.6.2. Remaining-Oil Mobilization in Heterogeneous Reservoirs

Once mobility control is established in dominant flow pathways, the remaining issue is whether redistributed flow can contact oil that was poorly swept during waterflooding. Figure 7d illustrates this process, in which part of the injected fluid is redirected from preferential channels toward under-swept regions containing remaining oil.

This mechanism is consistent with the reservoir heterogeneity shown in Figure 1 and the recovery behavior observed in Figure 5. High-permeability intervals had stronger water invasion, while medium- and low-permeability intervals retained higher oil saturation. In the core-flooding experiments, the largest polymer incremental recovery occurred in the medium-permeability core rather than in the high- or low-permeability core. This response suggests that remaining-oil mobilization requires two conditions at the same time: recoverable oil must still be present, and the polymer must be able to propagate sufficiently to modify the flow path. The field response in Figure 6, including reduced water cut, increased oil production, and progressive cumulative oil increment, provides larger-scale consistency with this interpretation.

Within this framework, hydrophobically associating polymer flooding improves recovery through a permeability-dependent mobility-control process. Associative thickening provides the fluid-property basis, pore-throat adaptation controls polymer propagation,

residual resistance modifies preferential flow paths, and redistributed flow mobilizes part of the oil retained in under-swept regions. The EOR effect is therefore better understood as the outcome of coupled solution behavior, porous-media interaction, and reservoir heterogeneity, rather than as a single-factor viscosity effect.

It should also be noted that the proposed mechanism was inferred from rheological parameters, pressure response, RF/RRF, recovery behavior, and field production consistency. Direct pore-scale visualization, in situ polymer-concentration mapping, or microscopic displacement imaging was not performed in this work. Therefore, the mechanism is presented as a quantitatively constrained interpretation of the observed responses, rather than as direct visual proof of microscopic displacement pathways.

The mechanism proposed in this study was mainly derived from heterogeneous sandstone cores and well-log-interpreted reservoir parameters. For reservoirs with more complex mineralogical heterogeneity, such as carbonate or coral reef limestone systems, polymer transport may also be influenced by mineral composition, pore-wall mechanical properties, dissolution-induced pore-throat evolution, and surface reactivity. Therefore, the present permeability-dependent mobility-control framework should be extended cautiously to highly soluble or strongly reactive mineral systems. In addition, nanofluid flooding studies indicate that wettability alteration, interfacial interaction, adsorption/retention, dispersion stability, and nanoparticle transport can also affect EOR performance. These mechanisms differ from the viscosity-enhancement and residual-resistance processes emphasized in this work, but they suggest that future EOR design in highly heterogeneous reservoirs may benefit from combining polymer mobility control with mineral-specific surface regulation or nanofluid-based interfacial control.

3.7. Practical and Economic Implications Compared with Other EOR Materials

From a practical and economic perspective, the evaluated polymer system has several advantages for field-scale mobility-control applications. First, the polymer is a commercially available hydrophobically modified partially hydrolyzed polyacrylamide-type material, and therefore does not require additional synthesis, nanoparticle functionalization, or complex dispersion procedures before field use. Second, the standard concentration used in this work was 0.25 wt%, which matched the field injection design and provided a measurable viscosity basis for mobility control without using an excessively high polymer dosage. Third, the field response showed that daily oil production increased from 11.6 to 20.4 t/d, water cut decreased from 93.1% to 81.6%, and the cumulative oil increment reached 2055 t after polymer injection. These results suggest that the economic value of the system is mainly associated with its field deployability, existing chemical-supply compatibility, and ability to improve sweep efficiency in heterogeneous reservoirs.

In addition to polymer cost and oil-displacement efficiency, produced-water reuse and injection damage are also important factors affecting the field economics and sustainability of polymer flooding. Recent work on alkali-free ternary composite flooding produced wastewater showed that suspended solids, oil droplets, and residual polymers in produced water may cause permeability damage during reinjection. Huang et al. reported that, for 200 mD cores, reinjection risk became significant when the oil content or suspended-solids content reached 60 mg/L, whereas an optimized polymer system prepared with alkali-free ternary produced water increased oil recovery by approximately 17%, indicating potential reservoir compatibility and resource-reuse value [18]. This finding suggests that field application of the present hydrophobically associating polymer should not be evaluated only from polymer viscosity, RF/RRF, and recovery increment, but also from injection-water quality, residual-polymer handling, produced-water reuse, and potential permeability

damage during reinjection. Therefore, future optimization should combine mobility-control performance with produced-water compatibility and reinjection-damage assessment.

Recent green nanocomposites and biopolymer-based nanocomposite systems have attracted increasing attention because they may improve oil recovery through wettability alteration, interfacial-tension reduction, disjoining-pressure modification, and emulsification. Some reported optimum cases show strong oil-displacement performance at relatively low nanoparticle concentrations. However, their practical application may require additional synthesis, dispersion stabilization, compatibility evaluation, and scale-up verification. Therefore, the comparison in Table 9 should not be interpreted as a direct ranking of material performance under identical conditions, because reservoir type, oil properties, salinity, temperature, flooding protocol, and recovery definitions differ among studies. Instead, it highlights the different application logic: green nanocomposites may provide strong microscopic displacement effects, whereas the present commercial hydrophobically associating polymer emphasizes field-ready mobility control and permeability-dependent sweep improvement.

Table 9. Comparison of the present polymer flooding system with representative EOR materials reported in previous studies.

EOR Material/System	Main Optimization or Evaluation Focus	Representative Reported Performance	Practical or Economic Consideration	Main Distinction from this Work
Present hydrophobically modified partially hydrolyzed polyacrylamide-type associating polymer	Mobility control in heterogeneous reservoirs; permeability-dependent RF/RRF and oil recovery	Medium-permeability core showed the highest polymer/post-polymer incremental recovery of 14.5 ± 0.8%; field cumulative oil increment reached 2055 t	Commercially available polymer; simple hydration and injection process; no nanoparticle synthesis or dispersion stabilization required	Focuses on field-relevant mobility control and reservoir heterogeneity constraints rather than new material synthesis
Conventional polymer flooding systems	Viscosity enhancement and mobility-ratio reduction	Generally effective for improving sweep efficiency, but performance can decline under high salinity, high temperature, and strong shear	Mature and relatively low-cost, but may require higher dosage or may suffer viscosity loss in harsh reservoirs	This work uses hydrophobic association to improve viscosity retention and residual resistance under heterogeneous conditions
Hydrophobically associating polymer systems	Salt tolerance, shear-responsive viscosity, and residual flow resistance	Reported to improve viscosity retention and residual resistance compared with conventional HPAM-type systems	More expensive than ordinary HPAM but still compatible with conventional polymer-flooding facilities	This work links polymer behavior with well-log-interpreted heterogeneity and field response
Alkali-free ternary composite flooding produced-wastewater system	Produced-water characteristics, injection damage, and oil-displacement efficiency during reinjection	For 200 mD cores, reinjection risk became significant when oil content or suspended solids reached 60 mg/L; the optimized polymer system prepared with produced water increased recovery by approximately 17%	Promotes produced-water reuse and reduces freshwater demand, but requires control of oil droplets, suspended solids, and residual polymers to avoid permeability damage	This work focuses on hydrophobically associating polymer mobility control; produced-water reuse and reinjection damage were not directly tested and should be considered in future field optimization
Green nanocomposites based on SiO_2/montmorillonite/xanthan-type systems	Wettability alteration and interfacial-tension reduction at optimized nanoparticle concentration	Reported tertiary recovery increments include approximately 11.72% in carbonate media and 15.79% in sandstone media under optimum nanocomposite conditions	Low nanoparticle dosage and potential environmental benefit, but synthesis, dispersion stability, and reservoir compatibility must be verified	These systems emphasize microscopic wettability/IFT control, whereas this work emphasizes mobility control and injectivity–resistance balance

Table 9. *Cont.*

EOR Material/System	Main Optimization or Evaluation Focus	Representative Reported Performance	Practical or Economic Consideration	Main Distinction from this Work
Aloe vera biopolymer/nano composite-type green systems	Green polymeric/ nanocomposite EOR with IFT reduction and wettability alteration	Some reported optimum formulations achieved high total oil recovery under laboratory conditions	Environmentally attractive, but may require additives such as alcohol, salts, or nanoparticles and further field-scale validation	Provides a green-material route, while this work provides a field-ready commercial-polymer route
TiO_2/quartz or metal-oxide nanocomposite systems	Wettability alteration, IFT reduction, and nanoparticle-assisted displacement	Some optimized nanofluids reported high oil recovery in laboratory plugs	Potentially strong microscopic displacement effect, but aggregation, retention, and injectivity risks need evaluation	Nanocomposites target interfacial and surface-force effects; this work targets permeability-dependent flow redistribution

Overall, the present system is not claimed to outperform all green nanocomposite materials under laboratory optimum conditions. Its practical significance lies in combining commercial availability, simple preparation, reservoir-condition stability, and field-scale production response. For heterogeneous high-water-cut reservoirs, this may be economically attractive because the additional oil increment is obtained through mobility-control improvement without introducing a more complex nanoparticle synthesis or stabilization process. However, from the viewpoint of field-scale sustainability, future implementation should also consider produced-water reuse, residual-polymer treatment, reinjection-water quality control, and permeability-damage risk. These factors may affect the net economic benefit of polymer flooding as strongly as polymer cost and laboratory oil-displacement efficiency.

It should be clarified that the field-application route proposed in this study is based on the hydrophobically modified partially hydrolyzed polyacrylamide-type associating polymer, rather than on a nanocomposite flooding system. The green nanocomposite systems discussed above were included only for literature comparison and as possible future extensions. For the present polymer system, field application would follow a conventional polymer-flooding procedure, including polymer hydration in compatible injection water or produced water, preparation at the field-designed concentration of 0.25 wt%, filtration, injection through the existing injection system, and monitoring by injection pressure, water cut, oil production, and cumulative polymer-injection volume. If nanocomposite-assisted polymer flooding is considered in future work, nanoparticle dispersion stability, adsorption/retention, injectivity damage, environmental compatibility, and scale-up feasibility should be evaluated before field use.

4. Conclusions

In summary, hydrophobically associating polymer flooding showed a clear permeability-dependent enhanced oil recovery response in heterogeneous porous media. The main contribution of this work is the establishment of a heterogeneity-constrained mobility-control framework linking well-log-interpreted reservoir parameters, polymer rheology, pore-throat transport, residual flow resistance, and field production response. The main conclusions are as follows:

1. The well-log-interpreted parameters revealed pronounced reservoir heterogeneity, with permeability varying from 7.9 to 186.5 mD. High-permeability layers showed higher water saturation, whereas medium- and low-permeability layers retained higher oil saturation, indicating a nonuniform sweep pattern after long-term water-flooding.

2. The polymer solution provided a stable fluid-property basis for mobility control under reservoir-relevant conditions. The 0.25 wt% solution showed a viscosity of 186.2 mPa·s at 7.34 s^{-1}, retained 139.5 mPa·s at 180,000 mg/L salinity, and maintained 74.9% viscosity retention after aging for 504 h.
3. Polymer injectivity, flow resistance, and recovery response were strongly controlled by core permeability. Although pressure gradient, RF, and RRF increased as permeability decreased, the medium-permeability core achieved the highest polymer/post-polymer incremental recovery of 14.5 ± 0.8%, indicating that effective EOR depends on balancing injectivity, residual resistance, and remaining-oil availability.
4. The field response was consistent with the laboratory-observed permeability-dependent mobility-control behavior. After polymer injection, daily oil production increased from 11.6 to 20.4 t/d, water cut decreased from 93.1% to 81.6%, and cumulative oil increment reached 2055 t after 18 months.

Overall, the findings indicate that polymer flooding in heterogeneous high-water-cut reservoirs should be evaluated as a coupled reservoir–fluid–porous-media process, rather than from bulk viscosity or flow resistance alone. This framework provides guidance for polymer selection, concentration optimization, and target-layer screening in field-scale mobility-control applications.

Author Contributions: X.Z.: conceptualization, methodology, data curation, formal analysis, investigation, visualization, writing—original draft, writing—review and editing; X.G.: supervision, methodology, resources, writing—review and editing; R.L.: data curation, investigation, field data collection, validation, writing—review and editing; F.Z.: resources, production data collection, project administration, writing—review and editing. All authors have read and agreed to the published version of the manuscript.

Funding: This research received no external funding.

Data Availability Statement: The original contributions presented in this study are included in the article. Further inquiries can be directed to the corresponding author.

Conflicts of Interest: Authors Rumin Liu and Fan Zhang were employed by China Oilfield Services Limited and The Fifth Oil Production Plant of Changqing Oilfield, respectively. The authors declare that the research was conducted in the absence of any commercial or financial relationships that could be construed as potential conflicts of interest.

Nomenclature

Symbol or abbreviation	Definition	Unit
EOR	Enhanced oil recovery	—
HPAM	Partially hydrolyzed polyacrylamide	—
RF	Resistance factor	—
RRF	Residual resistance factor	—
PV	Pore volume	—
ORF	Oil recovery factor	%
SD	Standard deviation	—
Q	Injection rate	mL/min
A	Core cross-sectional area	m^2
u	Darcy velocity	m/s
k	Core permeability	mD
ϕ	Porosity	fraction or %
$\dot{\gamma}$	Shear rate	s^{-1}
$\dot{\gamma}_{av}$	Apparent average pore shear rate	s^{-1}
τ	Shear stress	Pa

τ_0	Apparent yield stress	Pa
K	Consistency index	Pa·s^n
n	Flow behavior index	—
η	Apparent viscosity	mPa·s
η_t	Viscosity under a given salinity or aging condition	mPa·s
η_0	Reference viscosity under the corresponding initial or reference condition	mPa·s
V_{op}	Cumulative produced oil volume	mL
V_{OI}	Original oil volume in the core	mL
V_w	Produced water volume	mL
V_o	Produced oil volume	mL
ΔP_{w1}	Stable pressure difference during water preflush before polymer injection	MPa
ΔP_p	Stable pressure difference during polymer injection	MPa
ΔP_{w2}	Stable pressure difference during post-polymer waterflooding	MPa
$Q_{o,actual}$	Actual daily oil production after polymer injection	t/d
$Q_{o,baseline}$	Predicted baseline daily oil production without polymer injection	t/d
D	Exponential decline constant	month^{-1}

References

1. Seright, R.S.; Wang, D. Polymer flooding: Current status and future directions. *Pet. Sci.* **2023**, *20*, 910–921. [CrossRef]
2. Gbadamosi, A.O.; Junin, R.; Manan, M.A.; Yekeen, N.; Agi, A.; Oseh, J.O. Application of Polymers for Chemical Enhanced Oil Recovery: A Review. *Polymers* **2022**, *14*, 1433. [CrossRef] [PubMed]
3. Fu, H.; Bai, Z.; Guo, H.; Yang, K.; Guo, C.; Liu, M.; Liang, L.; Song, K. Remaining Oil Distribution Law and Development Potential Analysis after Polymer Flooding Based on Reservoir Architecture in Daqing Oilfield, China. *Polymers* **2023**, *15*, 2137. [CrossRef] [PubMed]
4. Sun, X.; Suo, L.; Wang, X.; Zhang, Y.; Wang, Y.; Liu, X.; Zhang, J. Study on the Occurrence Characteristics of the Remaining Oil in Sandstone Reservoirs with Different Permeability after Polymer Flooding. *Polymers* **2024**, *16*, 1902. [CrossRef] [PubMed]
5. Lu, X.; Cao, B.; Xie, K.; Cao, W.; Liu, Y.; Zhang, Y.; Wang, X.; Zhang, J. Enhanced oil recovery mechanisms of polymer flooding in a heterogeneous oil reservoir. *Pet. Explor. Dev.* **2021**, *48*, 169–178. [CrossRef]
6. Zhu, S.; Zhang, S.; Xue, X.; Chen, H.; Liu, Y.; Li, Y. Influencing factors for effective establishment of residual resistance factor of polymer solution in porous media. *J. Polym. Res.* **2022**, *29*, 210. [CrossRef]
7. Pinho de Aguiar, K.L.N.; Palermo, L.C.M.; Mansur, C.R.E. Polymer viscosifier systems with potential application for enhanced oil recovery: A review. *Oil Gas Sci. Technol.* **2021**, *76*, 65. [CrossRef]
8. Afolabi, R.O.; Oluyemi, G.F.; Officer, S.; Ugwu, J.O. Hydrophobically associating polymers for enhanced oil recovery—Part A: A review on the effects of some key reservoir conditions. *J. Pet. Sci. Eng.* **2019**, *180*, 681–698. [CrossRef]
9. Hassan, A.M.; Al-Shalabi, E.W.; Ayoub, M.A. Updated Perceptions on Polymer-Based Enhanced Oil Recovery toward High-Temperature High-Salinity Tolerance for Successful Field Applications in Carbonate Reservoirs. *Polymers* **2022**, *14*, 2001. [CrossRef] [PubMed]
10. Al-Hamairi, A.; AlAmeri, W. Development of a novel model to predict HPAM viscosity with the effects of concentration, salinity and divalent content. *J. Pet. Explor. Prod. Technol.* **2020**, *10*, 1949–1963. [CrossRef]
11. Afolabi, R.O.; Oluyemi, G.F.; Officer, S.; Ugwu, J.O. Hydrophobically associating polymers for enhanced oil recovery—Part B: A review of modelling approach to flow in porous media. *J. Mol. Liq.* **2019**, *294*, 111495. [CrossRef]
12. Yi, F.; Huang, B.; Wang, G. Hydrophobically Associating Polymers Dissolved in Seawater for Enhanced Oil Recovery of Bohai Offshore Oilfields. *Molecules* **2022**, *27*, 2744. [CrossRef] [PubMed]
13. Liu, T.; Chen, X.; Tang, X.; Wang, Y.; Li, H. Reservoir Compatibility and Enhanced Oil Recovery of Polymer and Polymer/Surfactant System: Effects of Molecular Weight and Hydrophobic Association. *Polymers* **2025**, *17*, 1390. [CrossRef] [PubMed]
14. Navaie, F.; Esmaeilnezhad, E.; Choi, H.-J. Effect of Rheological Properties of Polymer Solution on Polymer Flooding Characteristics. *Polymers* **2022**, *14*, 5555. [CrossRef] [PubMed]
15. Xu, Z.; Wang, H.; Liu, J.; Zhang, X.; Li, Y. Mechanisms of Mobility Control and Enhanced Oil Recovery by Polymer Flooding for Heterogeneous Reservoir. *Gels* **2025**, *11*, 854. [CrossRef] [PubMed]
16. Dou, X.; Zhang, H.; Liu, Y.; Wang, J.; Li, P. Study on the Viscosity Optimization of Polymer Solutions in Enhanced Oil Recovery. *Energies* **2022**, *15*, 9473. [CrossRef]

17. Zhang, Y.; Li, Z.; Wang, H.; Liu, X.; Chen, J. Experimental Study on the Enhanced Oil Recovery Mechanism of Polymer Flooding in Heterogeneous Reservoirs. *ACS Omega* **2023**, *8*, 12638–12649. [CrossRef] [PubMed]
18. Huang, B.; Shu, X.; Liu, X.; Fu, C.; He, J.; Zhang, X. Experimental study on the characteristics, injection damage, and oil displacement efficiency of alkali-free ternary composite flooding extracted wastewater. *Energy* **2025**, *332*, 137278. [CrossRef]

Disclaimer/Publisher's Note: The statements, opinions and data contained in all publications are solely those of the individual author(s) and contributor(s) and not of MDPI and/or the editor(s). MDPI and/or the editor(s) disclaim responsibility for any injury to people or property resulting from any ideas, methods, instructions or products referred to in the content.